Spatial deconvolution technique to improve the accuracy of reconstructed three-dimensional diffuse optical tomographic images

Harry L. Graber, Yong Xu, Yaling Pei, and Randall L. Barbour

A straightforward spatial deconvolution operation is presented that seeks to invert the information-blurring property of first-order perturbation algorithms for diffuse optical tomography (DOT) image reconstruction. The method that was developed to generate these deconvolving operators, or filters, was conceptually based on the frequency-encoding process used in magnetic resonance imaging. The computation of an image-correcting filter involves the solution of a large system of linear equations, in which known true distributions and the corresponding recovered distributions are compared. Conversely, application of a filter involves only a simple matrix multiplication. Simulation results show that application of this deconvolution operation to three-dimensional DOT images reconstructed by the solution of a first-order perturbation equation (Born approximation) can yield marked enhancement of image quality. In the examples considered, use of image-correcting filters produces obvious improvements in image quality, in terms of both location and μ_a of the inclusions. The displacements between the true and recovered locations of an inclusion's centroid location are as small as 1 mm, in an 8-cm-diameter medium with 1.5-cm-diameter inclusions, and the peak value of the recovered μ_a for the inclusions deviates from the true value by as little as 5%. © 2005 Optical Society of America

OCIS codes: 170.3880, 170.3010, 100.1830, 100.6950, 100.6890.

1. Introduction

The subject of this paper is a novel application of linear deconvolution techniques for the problem of improving the spatial resolution of three-dimensional (3D) reconstructed images in the field of diffuse optical tomography (DOT). In brief, DOT involves the illumination of tissue structures with one or more wavelengths of visible or near-infrared radiation at multiple positions on the tissue boundary, multiple-site detection of the light that is reemitted across the boundary, and reconstruction of images of the spatial distributions of the tissue's absorption or scattering coefficients. The clinical utility of DOT lies in the relations between these coefficients and physiological parameters such as blood oxygen saturation and tissue blood volume; furthermore, it is recognized that DOT offers specific practical advantages relative to established functional imaging modalities such as positron emission tomography and single-photon emission computed tomography (it does not entail administration of radionuclides) or functional magnetic resonance imaging (higher temporal resolution, possibly less ambiguity in the interpretation of results).

In a series of papers published during the past 4–5 years, our group has demonstrated the advantages of performing rapid repeated DOT measurements, then extracting dynamic information by applying various time-series analysis methods—many of which are already widely used to process optical spectroscopy data—to the reconstructed images.[1–7] As a practical matter, a requirement for use of these algorithms is the availability of a reconstruction algorithm that can recover many images in a short time. The basic framework we have adopted for this purpose is the normalized difference method (NDM),[8] which is robust to many of the biases and types of noise that are commonly encountered when laboratory or clinical DOT measurements are performed and is also able to accommodate many refinements. One of these, the normalized constraint method,[9] was shown to suc-

H. L. Graber (harry.graber@downstate.edu), Y. Xu, and R. L. Barbour are with the Department of Pathology, State University of New York Downstate Medical Center, Box 25, 450 Clarkson Avenue, Brooklyn, New York 11203. Y. Xu, Y. Pei, and R. L. Barbour are with NIRx Medical Technologies LLC, 15 Cherry Lane, Glen Head, New York 11545.

0003-6935/05/060941-13$15.00/0

cessfully distinguish absorption and scattering perturbations in a diffusing medium over a broad range of medium optical properties when applied to continuous-wave DOT measurement data. For cases in which the test medium for the normalized constraint method had spatially coincident absorption and scattering perturbations, we assessed the algorithm's ability to separate them by assigning a qualitatively different form of temporal fluctuation to each optical parameter.[10] These dynamics acted as tags by which interparameter cross talk was precisely quantified.

While the preceding study was in progress, it was recognized that the tagging of optical parameters with temporal information immediately suggests a general mechanism to characterize the action of DOT image reconstruction algorithms on their input data.[11–14] Namely, let a distinct mode of temporal fluctuation be assigned to each optical parameter of interest in every volume element of a medium, and let a time series of forward- and corresponding inverse-problem solutions be computed. Then a map of magnitude versus location for a given mode of fluctuation within the image space reveals precisely how the reconstruction algorithm distributes the corresponding optical parameter throughout that space. A mapping from object space into image space obtained in this way is conceptually analogous to a point-spread function (PSF),[15] which characterizes the physical accuracy and resolution of an optical device. In view of this analogy, the term information spread function (ISF) has been adopted as our descriptor for the type of object–space to image–space mapping described here.

The ISF formulation has an important implication that provides the main topic of the present paper. Namely, once the behavior of a reconstruction algorithm has been characterized under a given set of initial conditions (e.g., the NDM for a particular reference medium and arrangement of sources and detectors), its ISFs can be used in deconvolution computations to improve the spatial resolution and accuracy of reconstructed images. This application is analogous to the established practice in which the point-spread functions of an optical measuring device are used as the basis for calibration and correction procedures to reduce image blurring or aberrations.[16–19] Results presented in this paper demonstrate that highly significant improvements in the quality of DOT image spatial information can be achieved in this way. It is worth stressing that the technique described here can be applied to media of arbitrary shape and internal composition, and arbitrary source–detector geometries, in a computationally efficient manner.

It is well appreciated that solutions to the DOT forward problem are nonlinear functions of the medium's optical parameter values. Previously, groups that engaged in DOT research, ourselves included, always assumed that these nonlinearities are a principal cause of the distortions and low spatial resolution typically seen in images recovered by linear reconstruction algorithms.[20,21] Accordingly, the usual prescription used to improve image quality has been to adopt a nonlinear reconstruction strategy, recomputing solutions to the forward and inverse problems in an alternating pattern.[22] The findings presented here imply, however, that linear spatial convolution, or mixing of information from many target medium locations in any given image pixel or voxel, is actually a more important source of the errors in reconstructed DOT images. The significance and limitations of this premise are expanded on in Section 4.

2. Methods

A. Spatial Deconvolution Algorithm

The strategy described here was conceptually motivated by a consideration of the physical basis of image formation in magnetic resonance imaging (MRI). There, spatial discrimination is possible because the imposition of a magnetic field gradient creates a range of position-dependent resonance frequencies. This same concept is applied here to the image formation problem of optical tomography, although it seems likely (see Section 4) that it will be applicable to other inverse problems as well. The basic idea is that first-order solutions to linear perturbation problems often produce less than ideal solutions, with image blurring evident. Now suppose there is some way to specifically encode the pixel information in the object space and to track where it is recovered in the image space. As in MRI, this can be accomplished when the absorption coefficient (μ_a) is tagged in every object pixel with a unique time-varying function. The reduced scattering coefficient (μ_s') can be simultaneously tagged in the same way to assess the degree of interparameter cross talk in the recovered images. However, to simplify the presentation in this initial demonstration, only μ_a was modulated in the examples presented in this paper.

In the implementation that was used to produce the results presented below, the particular tagging functions used were simple sine waves with incommensurable frequencies. We achieved incommensurability by using the square roots of successive prime numbers as the tag frequencies (i.e., $f_{1, 2, 3, 4, \ldots}$ = 1, $2^{1/2}$, $3^{1/2}$, $5^{1/2}$, . . . Hz) so that the ratio of any two is an irrational number; by adopting this sequence, any nonlinear phenomena that might occur cannot produce harmonics or sum–difference frequencies that are equal to any of the tag frequencies. The tagging functions were evaluated at a large number N_t ($N_t = 16, 384 = 2^{14}$) of successive time points, with a constant time interval $\Delta t(\Delta t = 0.005$ s) that was short relative to the difference between the oscillation periods of the two highest-frequency tagging functions. This choice of N_t and Δt assures that none of the tagging functions are undersampled, which would produce aliasing artifacts, and that they all can be resolved in the frequency domain.

At each time point a forward problem for a tomographic measurement (i.e., multisource, multidetector) was solved, as described in Subsection 2.B. We
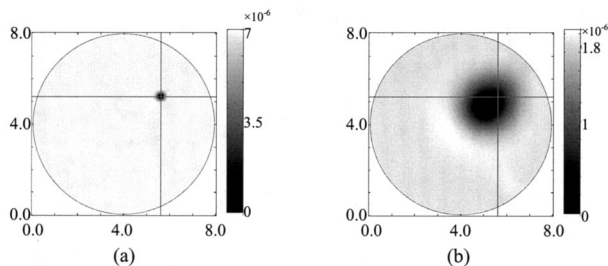
Fig. 1. (a) Spatial map of the amplitude of one selected temporal model function assigned to the absorption coefficient (μ_a) of a FEM mesh node located at the intersection of the horizontal and vertical lines. In this example, the mesh is an 8-cm-diameter 2D disk with homogeneous $\mu_s{}'$ and homogeneous time-averaged μ_a. (b) Spatial map of the amplitude in the time series of reconstructed μ_a images of the same temporal frequency as that assigned to the indicated FEM mesh node in (a).

subsequently solved the inverse problem, as described in Subsection 2.C, by using the NDM to produce a system of linear equations whose solution was computed by LU decomposition.[23] In this way a time series of reconstructed images was built up. Inspection of the power spectra of the images (i.e., spatial maps of power versus position for selected frequencies) directly identifies where and to what extent information from each pixel in the object domain is mapped to the image domain. As described in Section 1, a spatial map of this sort is referred to as an ISF. The details of the information spread, a two-dimensional (2D) example of which is shown in Fig. 1, are specific to the properties of the object and the illumination geometry used and to the algorithm employed for image recovery. Accordingly, inspection of these maps can provide valuable insight into the action of a reconstruction algorithm. The ISF in Fig. 1, for example, demonstrates that the reconstruction algorithm used yields images containing two commonly observed types of error. First, the optical parameter (absorption coefficient, in this example) value present at a specific location in the medium [Fig. 1(a)], as identified by the amplitude of the sinusoidal fluctuation used to tag its location, is attributed to a much larger area in the image space [Fig. 1(b)]. Second, the location of the high-amplitude peak in the image is displaced from its correct location toward, in this case, the center of the image space. That is, the reconstruction algorithm used here produces a blurred and distorted image.

The potentially most important application of the knowledge obtained when we compute ISFs would be to use them as the basis of an image enhancement algorithm. That is, knowing how optical parameter information is mapped from object space to image space should enable one to devise a suitable correction that would in effect remove the effects of linear spatial convolution from images. In practice, in the preferred strategy for doing this, we do not use the power spectra of the recovered temporal fluctuations (or, more generally, the temporal covariance between the assigned and recovered tagging func-

tions) as the input data for derivation of image deconvolution operators. The reason is that computation of the relevant deconvolution operator typically is an ill-conditioned problem. Consequently, for media comprising N_s voxels, our attempts to generate such operators by inverting $N_s \times N_s$ matrices of ISFs have mostly yielded unsatisfactory results.[12] (The issue of ill-conditioning is also important to understand why in practice the best corrections are obtained when $N_t \gg N_s$, as discussed in Subsection 4.B.) Instead, the assigned and recovered time-varying μ_a in all pixels should be compared in the time domain directly. That is, the input is collected into an $N_s \times N_t$ matrix **Y** and the reconstructed μ_a's are collected into an $N_s \times N_t$ matrix **X**, where the element y_{ij} is the assigned (tag) value of μ_a in voxel i at time j and the element x_{ij} is the recovered value of μ_a in voxel i at time j. The objective is to determine an $N_s \times N_s$ filter matrix **F** that will transform **X** into **Y**. That is, a solution to the equation $\mathbf{Y} = \mathbf{FX}$ is sought. This **F** will subsequently be applied to reconstructed experimental images in the hope of improving them. Thus if **u** is a particular reconstructed image of a test medium (i.e., a medium different from all the ones used to generate **F**), then $\mathbf{v} = \mathbf{Fu}$ is the corresponding corrected, or deconvolved, or filtered image.

In general **X** and **Y** are not square matrices, as $N_t \gg N_s$ in the situations of interest. For example, in the results to follow there were 982 or 984 voxels [i.e., finite-element method (FEM) mesh nodes] in the 3D media that were studied, which is more than an order of magnitude smaller than the number of time steps. Then **X** and **Y** cannot in general be inverted, and the equation $\mathbf{Y} = \mathbf{FX}$ cannot hold. This situation is common in statistical problems; the matrix equation represents N_t linear equations in N_s unknowns; and unless the coefficients are linearly dependent in some way, there is no exact solution. A commonly used strategy in these cases is to try to make the difference matrix $\mathbf{Y} - \mathbf{FX}$ as small as possible, in the least-squares sense. That is, the elements f_{ji} of **F** are chosen so that the quantity

$$I = \sum_{k=1}^{N_t} \sum_{j=1}^{N_s} \left(y_{jk} - \sum_{i=1}^{N_s} f_{ji} x_{ik} \right)^2, \qquad (1)$$

which is the sum of the squares of the errors in the individual terms when **Y** is approximated by **FX** is minimized. Setting the derivative of I with respect to each element of **F** equal to zero yields

$$\frac{\partial I}{\partial f_{ji}} = -2 \sum_{k=1}^{N_t} \left(y_{jk} - \sum_{l=1}^{N_s} f_{jl} x_{lk} \right) x_{ik} = 0, \qquad (2)$$

or

$$\sum_{k=1}^{N_t} y_{jk} x_{ik} = \sum_{k=1}^{N_t} \sum_{l=1}^{N_s} f_{jl} x_{lk} x_{ik}, \qquad \forall i, j. \qquad (3)$$
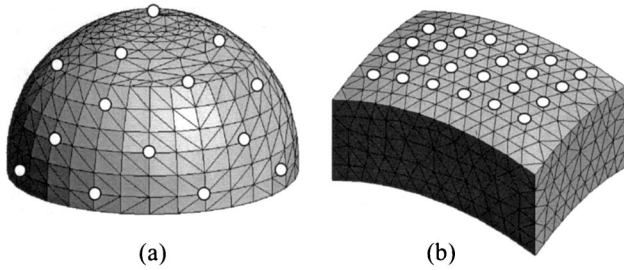
Fig. 2. Three-dimensional FEM meshes and source–detector geometries used to compute and test the image deconvolution operators. (a) Hemispheric mesh containing 982 nodes and 4309 elements. (b) Curved-slab mesh containing 984 nodes and 4274 elements. Source–detector locations are marked with small white circles.
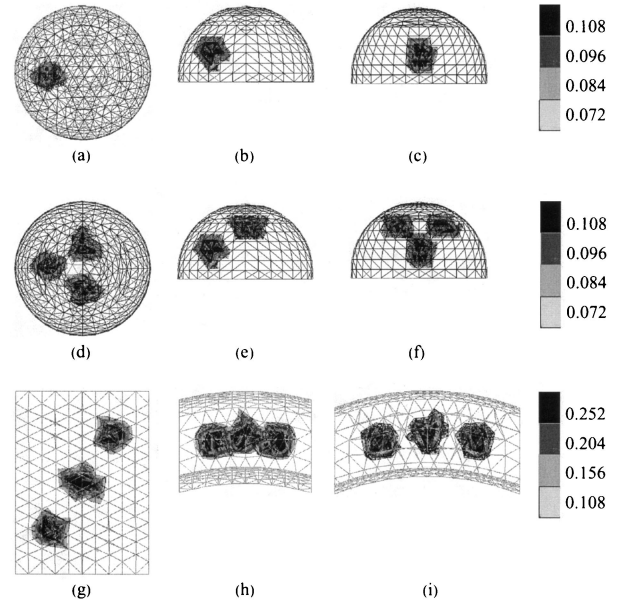

Fig. 3. Heterogeneous test media used in demonstrations of the efficiency of deconvolution to improve reconstructed image accuracy. (a)–(c) Hemisphere with one inclusion; (d)–(f) hemisphere with three inclusions; (g)–(i) curved slab with three inclusions. First column [(a), (d), (g)] shows the x–y projections; the second column [(b), (e), (h)] shows the x–z projections; and the third column [(c), (f), (i)] shows the y–z projections of the 3D test media. Numbers along the gray scales give the quantitative value of the spatially varying μ_a, whereas μ_s is homogeneous.

Equation (3) is just the matrix equation $\mathbf{YX}^T = \mathbf{FXX}^T$, where $\mathbf{X}^T$ is the transpose of $\mathbf{X}$. Since $\mathbf{XX}^T$ is a square matrix and the columns of $\mathbf{X}$ are linearly independent, $\mathbf{XX}^T$ can be inverted to give $\mathbf{F} = (\mathbf{YX}^T)(\mathbf{XX}^T)^{-1}$.

Finally, it should be noted that if the process is inverted, to produce the optimal approximation $\mathbf{X} = \mathbf{GY}$ in the least-squares sense, it is found that $\mathbf{G} = (\mathbf{XY}^T)(\mathbf{YY}^T)^{-1}$ and, in general, $\mathbf{F}$ and $\mathbf{G}$ are not inverses of each other.

B. Solution of the Forward Problem

Forward-problem solutions were computed for the two FEM meshes shown in Fig. 2. The hemispheric mesh shown in Fig. 2(a), which approximates the measurement geometry for DOT mammographic studies, contains 4309 tetrahedral elements with 982 nodes; the curved-slab mesh [Fig. 2(b)], which approximates the measurement geometry for DOT brain imaging, contains 4274 tetrahedral elements with 984 nodes. The diameter of the hemisphere is 8.0 cm. The distance between the convex and concave surfaces of the curved slab is 3 cm, and it can be circumscribed by a parallelepiped of dimensions 7.2 cm (length) $\times$ 5.2 cm (width) $\times$ 4.33 cm (thickness). The starting point in its generation was a 7.2 cm $\times$ 5.2 cm $\times$ 3.0 cm rectangular slab, which was next subjected to two thickness-preserving circular bends, first in the length dimension and then in the width dimension.

Defined sets of points on the convex mesh surfaces were used as the locations for isotropic sources or detectors. For the hemispheric mesh, 29 detector locations were designated [only 14 are visible in Fig. 2(a)], and 25 of these were also used as sources, for a total of 725 source–detector channels. For the curved-slab mesh, 24 source and detector locations were designated, as shown in Fig. 2(b), for a total of 576 source–detector channels.

We acquired tomographic data for the simulated tissue models by using the FEM to solve the diffusion equation with Robin boundary conditions and a dc source term. For a spatial domain Λ with boundary $\partial\Lambda$, this is represented by the expression

$$\nabla \cdot [D(\mathbf{r})\nabla\phi(\mathbf{r})] - \mu_a(\mathbf{r})\phi(\mathbf{r}) = -\delta(\mathbf{r} - \mathbf{r}_s), \quad \mathbf{r} \in \Lambda \quad (4)$$

where $\phi(\mathbf{r})$ is the photon intensity at position $\mathbf{r}$, $\mathbf{r}_s$ is the position of a dc point source, and $D(\mathbf{r})$ and $\mu_a(\mathbf{r})$ are the position-dependent diffusion and absorption coefficients, respectively. Here the definition used for the diffusion coefficient was $D(\mathbf{r}) = 1/\{3[\mu_a(\mathbf{r}) + \mu_s'(\mathbf{r})]\}$, where $\mu_s'(\mathbf{r})$ is the position-dependent reduced scattering coefficient. For all computations considered in this paper, both media shown in Fig. 2 had spatially homogeneous and temporally invariant scattering with $\mu_s' = 10$ cm^{-1}.

For the forward-problem computations that generated the object versus image comparisons that were used to compute filter ($\mathbf{F}$) matrices, the spatial distributions and temporal fluctuations of the dynamic, heterogeneous media's absorption coefficients are described in Subsection 2.A. The spatiotemporal mean value was $\langle\mu_a\rangle = 0.06$ cm^{-1}, and the amplitude of the sinusoidal temporal variation at each FEM mesh node was 0.0048 cm^{-1} (8%) for the hemisphere and 0.009 cm^{-1} (15%) for the curved slab. For the computations that generated the data used in the subsequent tests of the filters' image-correcting power, the static, spatially heterogeneous medium structures shown in Fig. 3 were employed. In this step the FEM meshes used for computation of detector readings intentionally were made finer than those used for generation of the $\mathbf{F}$ matrices and for subsequent image reconstruction (hemisphere, 2212 nodes and

10,305 elements; curved slab, 2062 nodes and 8698 elements) so that we would not be committing a simple inverse crime. In these test media the inclusions are approximately spherical (limited by the coarseness of the FEM meshes), with average diameters of 1.5 cm for the hemispheres and 1.2 cm for the curved slabs. The background regions of these media had uniform absorption, with $\mu_a = 0.06$ cm^{-1}, whereas the inclusions were more strongly absorbing, with $\mu_a = 0.12$ cm^{-1} for the hemisphere and either 0.12 cm^{-1} (Fig. 9) or 0.3 cm^{-1} (Figs. 6 and 8) for the curved slab. The latter perturbation was made larger strictly for reasons of computational convenience, i.e., because backscattering measurements were being simulated in this case and the inclusions' volumes were less by almost a factor of 2 [$(1.2$ cm$/1.5$ cm$)^3 = 0.512$], a higher value of μ_a in the inclusions was needed to produce detector reading perturbations of the same magnitude as those obtained for the hemispheric medium. However, it should be stressed—and the results presented in Fig. 9 prove—that the image reconstruction and image enhancement algorithms do not require this degree of contrast between structures in the medium to perform successfully.

Imaging operators (see Subsection 2.C) were computed, in the manner described in Ref. 24, for each source–detector channel. In brief, each row of the matrix $\mathbf{W}_r$ [Eq. (5)] is a function of two forward-problem solutions: a product of forward and adjoint intensities for perturbations of μ_a and a dot product of forward and adjoint intensity gradients for perturbations of D. For each simulated medium (i.e., target medium) shown in Fig. 2, a single set of imaging operators was used for all inverse-problem computations. These were computed for a homogeneous reference medium having the same shape, size, and measurement geometry as the (heterogeneous) target and with optical parameters equal to the mean values ($\mu_a = 0.06$ cm^{-1}, $\mu_s' = 10$ cm^{-1}) of those in the target.

C. Solution of the Inverse Problem

The reconstruction algorithm that was used to generate the results presented below seeks to solve a modified perturbation equation whose form is

$$\mathbf{W}_r \cdot \delta\mathbf{x} = \delta\mathbf{I}_r, \tag{5}$$

where $\delta\mathbf{x}$ is the vector of differences between the optical properties [e.g., absorption and scattering (diffusion) coefficients] of a target and a defined reference medium; $\mathbf{W}_r$, the imaging operator or weight matrix, is the weight matrix describing the influence that each voxel has on the surface detectors for the selected reference medium; and $\delta\mathbf{I}_r$ is proportional to the difference between detector readings obtained from the target in two distinct states (e.g., the difference between data collected at two different instants or the difference between instantaneous and time-averaged data). Also, to improve the condition number of the linear systems being solved, zero-order

Tikhonov regularization (ridge regression) was used in all image reconstructions. Thus we reconstructed the images not by computing $\delta\mathbf{x} = \mathbf{W}_r^{+} \cdot \delta\mathbf{I}_r = \mathbf{W}_r^{T}(\mathbf{W}_r\mathbf{W}_r^{T})^{-1} \delta\mathbf{I}_r$ in accordance with Eq. (5), but by computing the regularized quantity

$$\delta\mathbf{x} = \mathbf{W}_r^{T}(\mathbf{W}_r\mathbf{W}_r^{T} + \lambda\mathbf{I})^{-1}\delta\mathbf{I}_r. \tag{6}$$

For all inverse-problem calculations carried out for this paper, the numerical value of the regularization parameter was $\lambda = 0.01$. As is shown subsequently, the presence of regularization term is important, but the parameter value used has, over a 5 order-of-magnitude range from $\lambda = 10^{-5}$ to $\lambda = 10^0$, little effect on image quality.

The distinction between Eqs. (5) and (6) and a standard linear perturbation equation lies in the structure of the right-hand side. Here we used the previously described NDM,[8] in which the quantity $\delta\mathbf{I}_r$ on the right-hand sides of Eqs. (5) and (6) is defined by

$$(\delta\mathbf{I}_r)_i = \frac{(\mathbf{I} - \mathbf{I}_0)_i}{(\mathbf{I}_0)_i} (\mathbf{I}_r)_i. \tag{7}$$

In Eq. (7), $\mathbf{I}_r$ is the computed detector readings corresponding to a selected reference medium. For the filter-generating computations, $\mathbf{I}$ and $\mathbf{I}_0$ represent the intensity at a specific time point and the time-averaged intensity, respectively. For the filter-testing computations, $\mathbf{I}$ and $\mathbf{I}_0$ are the intensities (i.e., detector readings) computed for the heterogeneous target medium and the homogeneous reference medium, respectively.

A Levenberg–Marquardt (LM) algorithm was used to compute the numerical solutions to Eq. (6).[22] A time period of less than 1 min was required for computation of the weight matrix and the subsequent LU decomposition. [Note that the L (lower triangular) and U (upper triangular) factors could be read from a library of precomputed matrices and that the decomposition is a one time only event in any case.] Subsequently, the time required to reconstruct each image (i.e., backsubstitution step) was approximately 0.3 s on a PC with a 2.4-GHz Pentium IV processor and 1 Gbyte of RAM. The weak dependence of image quality on the degree of regularization used, for $\lambda \geq 10^{-5}$, is shown in Fig. 4, where the root-mean-squared error (RMSE) of the reconstructed image relative to the original target medium is plotted versus λ for the three-inclusion hemispherical medium depicted in Figs. 3(d)–3(f). For the uncorrected images that we reconstructed by solving Eq. (6) (dashed curve), the RMSE increases rapidly with decreasing λ for $\lambda < 10^{-6}$. However, the RMSE is only ~10% larger at $\lambda = 10^0$ than at the absolute minimum of the curve, which occurs at $\lambda = 5 \times 10^{-5}$. The dependence of RMSE on λ is even weaker for the corrected images (solid curve) and actually decreases with increasing λ over the same interval in which the un-
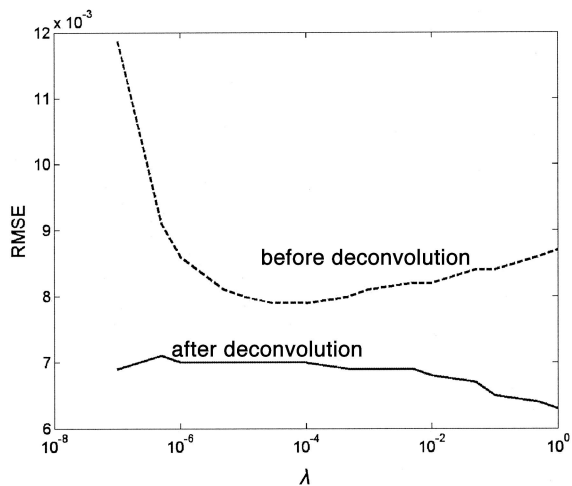
Fig. 4. Root-mean-squared difference between the three-inclusion hemispherical medium shown in Figs. 3(d)–3(f) and the uncorrected (dashed curve) and corrected (solid curve) reconstructed images of the same target, versus the magnitude of the Tikhonov regularization parameter λ.
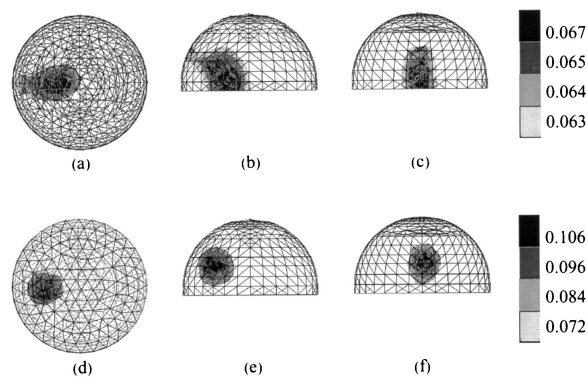

Fig. 5. Reconstructed image of one-inclusion hemispheric test medium [see Figs. 3(a)–3(c)]. (a)–(c) Uncorrected image, which is the solution to Eq. (6); (d)–(f) corrected image obtained by applying the spatial deconvolution to the result in (a)–(c). First column [(a) and (d)] shows the x–y projections; the second column [(b) and (e)] shows the x–z projections; and the third column [(c)–(f)] shows the y–z projections of the 3D images. Numbers along the gray scales give the quantitative value of the spatially varying μ_a.

corrected image RMSE increases. The specific value, $\lambda = 10^{-2}$, that we used in generating the results presented in Section 3 was chosen as a compromise value. Also worthy of note is the absence of crossings between the curves in Fig. 4, which indicates that there is no degree of regularization for which deconvolution fails to enhance the reconstructed image. Consistent with this, inspection of the uncorrected images (not shown) reveals that no value of λ yields reconstructed images substantially better than those presented below in Figs. 6(a)–6(c).

Initial tests of the spatial deconvolution strategy for image enhancement were made on noise-free data. Subsequently, to assess the robustness of the method to noise in detector data, the same image reconstruction and deconvolution steps were applied a second time to the media in Figs. 3(b) and 3(c), after the detector readings were corrupted with multiplicative Gaussian noise, at a uniform level of 1%. Thus the noise vector element corresponding to the ith source–detector channel was sampled from the Gaussian distribution $N[0, 0.01(\mathbf{I}_0)_i]$. Then $\mathbf{I}' = \mathbf{I} + \mathbf{n}$, where $\mathbf{n}$ is the noise vector, was substituted for $\mathbf{I}$ in Eq. (7).

3. Results

Three orthogonal 2D projections of the hemispheric target medium used in the first test of the spatial deconvolution approach are shown in Figs. 3(a)–3(c). The corresponding views of the image reconstructed obtained by the solution of Eq. (6) are shown in Figs. 5(a)–5(c). It can be seen that the presence, location, and direction (i.e., inclusion more strongly absorbing than background) of the inclusion are recovered reasonably accurately, whereas more quantitative features such as its shape and volume and the magnitude of the μ_a contrast are not. Noteworthy is the frequently seen tendency of some DOT image

reconstruction algorithms to push the recovered perturbation into regions of the medium with the lowest weight, which in this case lies along the planar boundary of the hemisphere. The same views of the corrected image obtained by application of the filtering scheme described here is shown in Figs. 5(d)–5(f). The improvement in image quality and the similarity between the image and the original target are striking. Comparison of the gray scales of the uncorrected and corrected images with those of the original reveals that the improvement is quantitative and demonstrates the possibility of accurately recovering the absolute value of optical parameter variations with a reconstruction algorithm that operates on relative changes in detector readings. Because of space limitations, extensive numerical analyses of qualitative and quantitative accuracy[10,25] are not presented here, but will be included in a more in-depth report currently in preparation. We do note here, however, that in this example the location of the inclusion's centroid in the corrected image lies within 1 mm of its true position, and the peak recovered μ_a lies within 5% of the correct quantitative value.

Although the preceding single-inclusion study might lead some to conclude that the quality of the uncorrected image is adequate, and the computational effort that went into generating the filter matrix is therefore gratuitous, it does not address the important issue of the reconstruction algorithm's resolving power. To examine the effect of our image-correcting procedure on this feature, the next test medium that was considered contained three inclusions, as shown in Figs. 3(d)–3(f). Here the average distance between the centroids of pairs of inclusions was 2.68 cm. The image that we reconstructed by using the method of Subsection 2.C, shown in Figs. 6(a)–6(c), exhibits the same types of quantitative inaccuracy as was seen in the one-inclusion case, but here the qualitative accuracy also suffers as a conse-
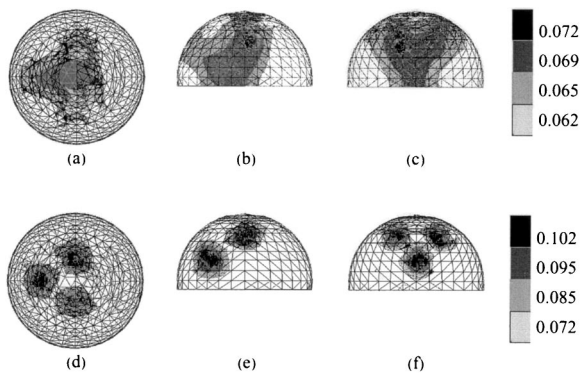
Fig. 6. Reconstructed image of a three-inclusion hemispheric test medium [see Figs. 3(d)–3(f)]. See caption to Fig. 5 for explanation of gray scales and of row and column assignments.
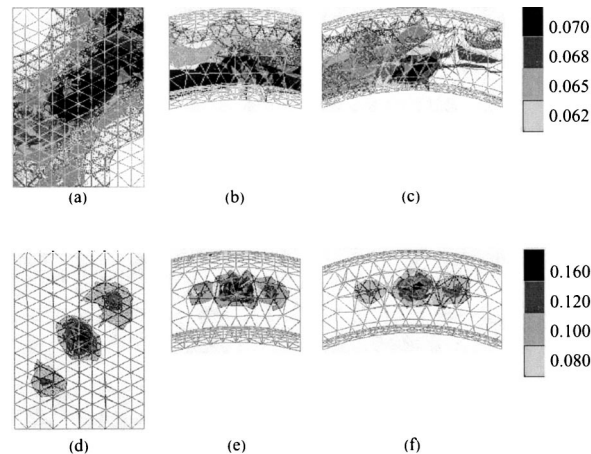

Fig. 7. Reconstructed image of a three-inclusion curved-slab test medium [see Figs. 3(g)–3(i)]. See caption to Fig. 5 for explanation of gray scales and of row and column assignments.

quence of the inability of the reconstruction to resolve the perturbation into three distinct objects. In contrast, the corrected image displayed in Figs. 6(d)–6(f) exhibits the same degree of qualitative and quantitative accuracy improvement as obtained in the one-inclusion case. Significantly, there is no appreciable degradation in the performance of the filtering strategy, even though the strongly absorbing volume is larger and the potential for nonlinear interactions among the inclusions exists in this case.[20,21] This observation suggests that the primary cause of inaccuracies in the uncorrected images produced with the solution of Eq. (6) are a consequence of linear spatial convolution arising from the algorithm's ISF. It is reasonable to suppose that a similar result would be obtained with a different choice of reconstruction algorithm, in which case the conceptual basis of nonlinear iterative reconstruction schemes would be called into question (see Section 4).

In the preceding two tests, the uncorrected images were reconstructed from fully tomographic sets of measurement data. Two important questions not yet addressed are the dependence of the filtering strategy's performance on the geometry of the target medium and on the disposition of sources and detectors (i.e., measurement geometry). To begin to examine these issues, the image-correction procedure was applied in the case of the three-inclusion curved-slab test medium shown in Figs. 3(g)–3(i). Here the distance between centroids of adjacent inclusions was 2.23 cm, and all three lay at the same depth. Consequently, nonlinear phenomena ought to have a smaller effect on the quality of the reconstructed image here than in the preceding hemispheric medium case. However, the quality of the image we recovered by using the method of Subsection 2.C is, as can be seen in Figs. 7(a)–7(c), so poor as to make it unusable. Application of the image-correcting filter appropriate for this case produces the result in Figs. 7(d)–7(f). The corrected image has the same levels of qualitative and quantitative accuracy as that obtained in the preceding tests, which means that an appreciably higher degree of improvement was obtained. The results in Figs. 7(d)–7(f) imply that information regard-

ing the correct spatial distribution of μ_a in the target medium is present in the uncorrected image, but in a highly spatially convolved form. This strengthens the hypothesis that nonlinear image-correction approaches, when applied to DOT problems, are based on a false premise regarding the origin of the inaccuracies in the reconstructed images. It further suggests (see Section 4) that many apparent DOT image reconstruction failures actually have been unrecognized successes, requiring only an appropriate post-processing step to put them into a visually recognizable form.

Because the preceding results were obtained under ideal conditions, it is important to examine the effect of factors that impair the quality of real experimental data on the effectiveness of the spatial deconvolution procedure. Chief among these is the inevitability of some level of random error in the detector readings used by the image reconstruction algorithm. In other medical imaging fields, it has been shown that deblurring operations can amplify image degradation resulting from noise.[26,27] Therefore it is important to include test cases in which noise was added to the detector data and to compare the output of the image-correction scheme to the corresponding noise-free result. The uncorrected and corrected images obtained of the three-inclusion hemispheric [Figs. 3(d)–3(f)] and curved-slab [Figs. 3(g)–3(i)] test media when the detector readings were corrupted with multiplicative noise as described in Subsection 2.C are shown in Figs. 8 and 9, respectively.

Comparing Figs. 8(d)–8(f) with Figs. 6(d)–6(f), it can be seen that the noise does not appreciably affect the accuracy of either qualitative or quantitative features of the recovered inclusions. Rather, the only apparent effect of noise is to introduce a number of irregularly shaped blobs of spurious μ_a contrast into the background region. That is, although noise places limits on spatial resolution and sensitivity, just as it does for any other imaging modality (i.e., inclusions with physical dimensions or contrast smaller than
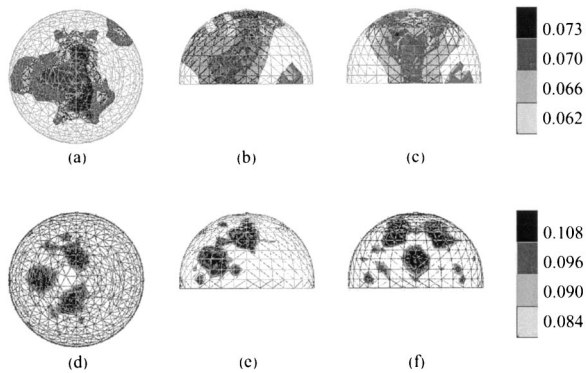
Fig. 8. Reconstructed image of three-inclusion hemispheric test medium [see Figs. 3(d)–3(f)] when detector data are corrupted with noise in the manner described in Subsection 2.C. See caption to Fig. 5 for explanation of gray scales and of row and column assignments.

Fig. 10. Comparison of the performance of the nonlinear iterative image reconstruction algorithm and the spatial deconvolution approach. The test medium is a curved slab with three inclusions [see Figs. 3(g)–3(i)]; detector data are noise free. See caption to Fig. 5 for explanation of gray scales and of row and column assignments.

those of the noise blobs cannot be distinguished from the effects of noise), it does not pose any extra burden on the image-correcting filter approach outlined here.

For the curved-slab case, a comparison of Figs. 9(d) and 7(d) could suggest that noise has a larger effect on the ability of the filtering scheme to resolve inclusions and to accurately recover their qualitative shape features. However, the views of the images that show the depth dependence of the recovered μ_a spatial distributions [Figs. 7(e) and 7(f) and 9(e) and 9(f)] reveal that the inclusions actually are well resolved. Also interesting is that the spurious blobs produced by the data noise have a marked depth dependence, and in this example most of them lie in the region more superficial than the inclusions. It is important to determine, in future research, whether this observation continues to hold when the relative noise level increases with increasing source–detector separation,[28] as one would expect to find in experimental or clinical data. If results of the type seen in

Fig. 9 are obtained consistently, then in subsequent efforts to incorporate regularization into the deconvolution step (in addition to the Tikhonov regularization that is used, as described in Subsection 2.C, to reconstruct the uncorrected images), the idea of employing a depth-dependent regularization functional should be explored. The regularization magnitude would increase with decreasing depth, as some previous empirical studies already have recommended.[29]

Finally, because a principal conclusion drawn from this study is that image-correcting procedures of the type presented here should either replace or complement the strategy of iteratively updating the forward- and inverse-problem computations, it is important to directly compare the performance of these two approaches when they are applied to the same set of detector data. The curved-slab target medium used for this comparison has the same anatomical structure as that shown in Fig. 3(b), but here the inclusion/background μ_a contrast ratio is 2:1, instead of the 5:1 used for the computations whose results are shown in Figs. 7 and 9. The first-order reconstructed image (not shown) is qualitatively similar to that in Figs. 7(a)–7(c), and the image recovered after ten iterations of a previously described[22] LM algorithm is shown in Figs. 10(a)–10(c). The total computation time was approximately 90 min on the same computing platform used for the filter generation and spatial deconvolution computations. Although evidence of a three-inclusion structure is present here, only two inclusions are well defined in terms of shape and centroid location, and only one has a well-defined boundary. It also can be seen that the error in the apparent depth of the inclusions is not corrected after this number of iterations. The corresponding result that we obtained by deconvolving the first-order image is shown in Figs. 10(d)–10(f). In this result all three inclusions are well resolved with well-defined boundaries, and their depth is correctly identified.
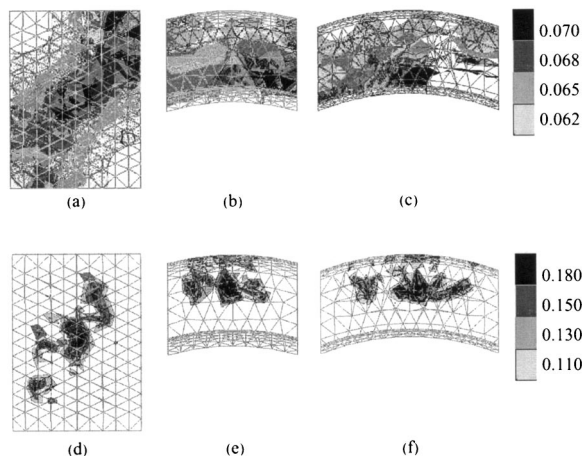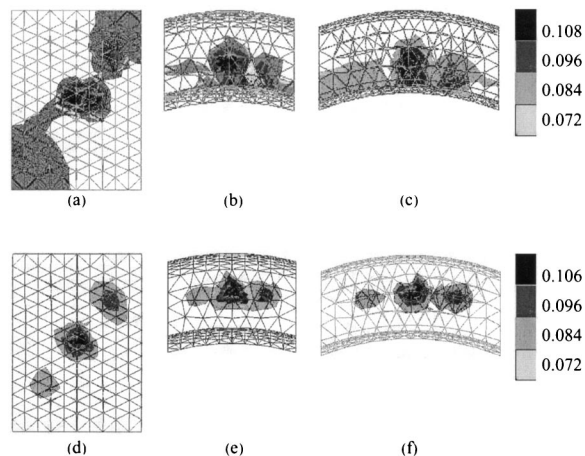

Fig. 9. Reconstructed image of three-inclusion curved-slab test medium [see Figs. 3(g)–3(i)] when detector data are corrupted with noise in the manner described in Subsection 2.C. See caption to Fig. 5 for explanation of gray scales and of row and column assignments.

It is recognized that the particular iterative reconstruction algorithm used in this example has not been optimized with respect to the convergence rate for the imaging problem that was considered. Undoubtedly the quality of the image in Figs. 10(a)–10(c) would improve with more iterations, and it is probable that algorithms can be found that require fewer iterations for convergence. In any case, the time required to recover the final answer would be many times greater than the ~ 0.01 s needed to apply the filter correction. In marked contrast to iterative strategies, the time required for filter generation can precede the collection of any given data set and so does not affect the time interval between data collection and production of the final image.

4. Discussion

In this paper a straightforward spatial deconvolution operation is presented that seeks to invert the information-blurring property of first-order perturbation algorithms for DOT image reconstruction. The computation of such a deconvolving operator, or filter, involves the solution of a large system of linear equations, in which known true distributions and the corresponding recovered distributions are compared. The application of a filter is by simple matrix multiplication. Thus, although their generation entails significant computational effort, for any given type of DOT measurement they can be precalculated, and only the application time ($\sim 10^{-3}$ s or 6–7 orders of magnitude smaller than the generation time for the illustrative examples presented here) contributes to the postmeasurement computational burden.

The method that was developed to generate the image-correcting filters was conceptually based on the frequency-encoding process used in MRI. It is largely for this reason that, for the examples presented in this paper, we tagged each medium's voxels by assigning incommensurable sinusoidal fluctuations to their optical coefficients. Because of this particular choice of tagging functions, the technique we developed for generating the filters was referred to in preliminary reports as frequency encoding of spatial information.[11,13] In general, however, many other functional forms should be usable for this purpose. Consequently, the generic term we apply to procedures of the type described above in Subsection 2.A is temporal encoding of spatial information.

A seemingly cogent objection to the strategy presented here can be raised, namely, that the inaccuracies and artifacts that the described spatial deconvolution corrects for are only those that the reconstruction algorithm itself introduces into the image. Then the appropriate remedy should be to substitute a better one, or at least to make a better choice of control variables (e.g., the optical parameters assigned to the reference medium or initial guess, regularization parameters, truncation point in a truncated singular value decomposition algorithm, whether and how to scale rows or columns of $\mathbf{W}_r$), rather than to attempt *a posteriori* repair on the output of one that is bad or suboptimally tuned. There is a three-part answer to this objection: First, nothing more is being claimed for our image enhancement procedure than that it can substantially improve results obtained when linear reconstruction techniques are used, but that the image quality attainable by these methods may not have been fully appreciated by some in the DOT community; second, that the reconstruction algorithm used may have properties (e.g., speed, robustness) that compel its use and are lacking in other algorithms that yield more accurate answers under ideal conditions[8–10]; third, that in practice it may not be possible to know in advance what the optimal values for all control variables are, so that an efficient data-driven technique for *a posteriori* correction has considerable practical value.

The specific application area of primary interest to our group is diffuse optical tomography. However, the strategy developed and presented here can be expected to have applicability to a much larger set of problem areas. This follows from the fact that there are many fields in which a linear transformation is used to convert sets of observations or measurements into interpretable results. A correction operation analogous to that derived here for the specific case of DOT should be possible in many of these areas. Electrical impedance tomography, microwave tomography, magnetoencephalographic imaging, and positron emission tomography and single-photon emission computed tomography are medical imaging modalities that could be expected to benefit from these operations, and they might also be usefully applied to inverse problems in electroencephalography. The potential for application to problem areas in geology, oceanography, atmospherics and meterology, and astronomy, wherein interpretation of observations also ultimately entails a solution to an inverse problem derived from a transport equation, also seems clear. Outside of the natural sciences, however, it also would seem that there is potential utility for the general correction strategy outlined here in economics and other social sciences, where, interestingly, inverse diffusion problems also are considered.[30,31]

A. Summary and Implications of Results

Here it has been shown that application of the deconvolution operation to DOT images reconstructed by a solution to a first-order perturbation equation (Born approximation) can yield marked enhancement of image quality. These corrected (filtered) images are quantitatively accurate in terms of target location, size, and shape. In the 3D examples that are considered here, use of image-correcting filters produced obvious improvement in image quality in terms of both location and μ_a of the inclusions. The displacements between the true and the recovered locations of an inclusion's centroid location were as small as 1 mm, in an 8-cm-diameter medium with 1.5-cm-diameter inclusions, and the peak value of the recovered μ_a for the inclusions deviated from the true value by as little as 5% (see Figs. 5, 6, and 8).

Multiple inclusions were present in all but one case, and in all of these the spatial deconvolution strategy successfully resolved the inclusions while also accurately locating each one.

Corruption of the simulated detector data with multiplicative Gaussian noise (Figs. 8 and 9) did not bring about a reduction of spatial resolution or in the qualitative (centroid location) or quantitative (peak μ_a value) accuracy of the recovered inclusions. Thus it is reasonable to progress from simulation studies to tests involving laboratory phantoms to determine whether the approach presented here is likewise robust to all the forms of noise that are present in experimental data. The principal effect of the noise was the appearance of small, irregularly shaped regions of spurious absorption contrast. Notably, for the case in which a backreflection measurement was simulated (Fig. 9), the latter regions showed a pronounced depth dependence, decreasing in size and magnitude with increasing depth. This pattern suggests that it could be profitable to implement depth-dependent regularization when Eq. (6) is solved or to combine the deconvolution step with a long-pass spatial-frequency filtering operation having a depth-dependent threshold.

The relatively low spatial resolution of recovered images in DOT applications has been observed and commented on many times. Also well known is the tendency of image reconstruction algorithms to produce appreciable error in the depth component of an inclusion's location, although the direction of the bias is a function of the specific algorithm that is employed. An important implication of the results in Figs. 5–9 is that much previous research on developing and improving image reconstruction algorithms has been based on a mistaken premise regarding the origin of these phenomena. We believe this point is one of the more significant conclusions of the present study and that some elaboration is called for here.

It is certainly true that if a perturbation in the optical coefficients of a medium is large in terms of magnitude or volume, then the first derivatives that constitute the imaging operator do not correctly model the effect of changes in the medium's optical coefficients on the detected near-infrared signals. Nonlinear reconstruction strategies proceed from the assumption that the inaccuracies in the images recovered by solution of the first-order perturbation equations are caused by these deviations from linear relationships between perturbation and signal. But if that assumption were correct, then the linear spatial deconvolution approach developed here would not be expected to enhance the accuracy of the test medium images, and in fact should make them worse. The quality of the results actually obtained, particularly in the direct comparison of spatial deconvolution and a nonlinear LM reconstruction algorithm (Fig. 10), implies that the information-spreading properties of the reconstruction algorithm are the true cause of the low spatial resolution and depth bias commonly seen in DOT images. It is recognized that ten is almost certainly not the optimum number of LM iterations;

employing the optimal number of iterations would improve the quality of the result in Figs. 10(a)–10(c), and the algorithm itself could probably be adjusted to yield a higher rate of convergence. In any case, the postmeasurement computational time and cost would invariably be many times greater for any approach of this type than for application of the image-correcting filter, which requires only a matrix multiplication.

The preceding is not an assertion that nonlinear relationships between optical parameter perturbations and detector readings are not present, or that they cannot in certain cases place important limits on the performance of linear reconstruction algorithms. In fact, we have explored the relative importance of linear information spread and nonlinear effects and have found (results not shown) that with sufficient effort the filtering strategy can be made to fail. In the test media for which this occurred, the inclusions were located at more than one depth, with superficial ones obstructing every source–detector channel's view of the deep ones. In at least some cases it was found that the nonlinear reconstruction algorithm eventually recovered all the inclusions, and the filtering approach recovered only the superficial ones. It is noteworthy, however, that in every such case eliminating the deep-lying inclusions from the medium had only a very small effect on the detector data (i.e., at best in the third significant digit). Then the addition of even a low level of noise or any sort of systematic error (i.e., the tests were all carried out on ideal, noise-free data) would bring us back to the situation in which the linear and nonlinear algorithms produce comparable answers.

An important implication of these considerations, as already alluded to, is that many earlier assessments of DOT reconstructed images, if based principally or exclusively on visual inspection of the images, may have been unduly pessimistic. An especially vivid example of this phenomenon can be seen in Fig. 7 (others almost as striking can be seen in Figs. 4 and 6 of Ref. 12). Here the first-order image obtained from a multiple-inclusion test medium has almost no hint of the actual structure of the medium, but the corrected image demonstrates that the correct answer is actually present in the former result, only in a visually unrecognizable form. It is our expectation that application of the appropriate spatial deconvolution operator to apparently unsatisfactory image reconstruction results obtained by many of the groups engaged in DOT research would have a comparably gratifying outcome. (In the future we hope to invite other groups to allow us to apply spatial deconvolution to some examples of their image data as a test of the preceding prediction.)

B. Theoretical and Numerical Considerations

There are several useful ways to conceptualize the method used to determine $\mathbf{F}$ that is outlined in Subsection 2.A. For one, it can be thought of as a particular type of general linear model calculation, in which the columns of $\mathbf{X}$ are the models that are pos-

tulated to account for most of the variability in each column of $\mathbf{Y}$ (i.e., $\mathbf{X}$ is the general linear model design matrix). Limiting our consideration to linear combinations of the models (i.e., main effects) is equivalent to assuming that interactions among two or more of them are unimportant. In principle, we could obtain a mapping from $\mathbf{X}$ into $\mathbf{Y}$ that is accurate over a larger range of medium optical coefficient values by solving higher-order equations,

$$\mathbf{y}_i = a_i + \sum_{j=1}^{N_s} b_{ij}\mathbf{x}_j + \sum_{j=1}^{N_s}\sum_{k=j}^{N_s} c_{ijk}\big[x_{j1}x_{k1} \ \ x_{j2}x_{k2} \ \ \ldots \ \ x_{jN_t}x_{kN_t}\big]^T + \ldots, \tag{8}$$

for the unknown coefficients a_i, b_{ij}, c_{ijk}, ... But to do so is a practical impossibility because of the prohibitively large number of additional terms, even if only two-way interactions are included in the model. Alternatively, the generation of $\mathbf{F}$ can be thought of as a system calibration problem, more computation intensive but no different in principle from common laboratory practices such as use of standard compounds with well-established melting points to produce a correction curve for a thermometer. Another alternative is to regard $\mathbf{X}$ and $\mathbf{Y}$ as the equivalent of a training set in a neural network computation and $\mathbf{F}$ as the equivalent of the connectivity pattern that results from the training process.

From any of the preceding interpretations for the filter generation process, one can infer the principal trade-off that must be borne in mind when specifying $\mathbf{Y}$: The set of modeled target media must constitute a representative sample of the mathematical space of all media to which the filter could possibly be applied; but at the same time, the magnitudes of the assigned perturbations cannot be so large that the relationship between the modeled and the recovered optical coefficients becomes manifestly nonlinear. (Of course, it is understood that this trade-off places a limit on the range of target medium optical coefficients for which a computed filter can have its image-correcting effect.) In Fig. 11 we illustrate what is meant by representative sample; points whose coordinates are the absorption coefficient values of two particular FEM nodes in the first 1000 time points of the curved-slab training set are plotted in Fig. 11(a), and the corresponding plot for the entire 2^{14}-point time series is plotted in Fig. 11(b). These plots are 2D projections of the 984-dimensional mathematical space (μ_a space) whose points correspond to all possible distributions of μ_a in the curved slab. The plot in Fig. 11(b) makes it clear that, as the size of the training and calibration set increases, it will contain at least one point that falls within any specified finite subregion of μ_a space. Equivalently, a sufficiently large training set guarantees the existence of a training set point lying arbitrarily close, in μ_a space, to any given test medium.

The preceding considerations provide an important part of the answer to the question of why it was necessary that N_t be almost 17 times larger than N_s in the filter-generating process, when intuitively it
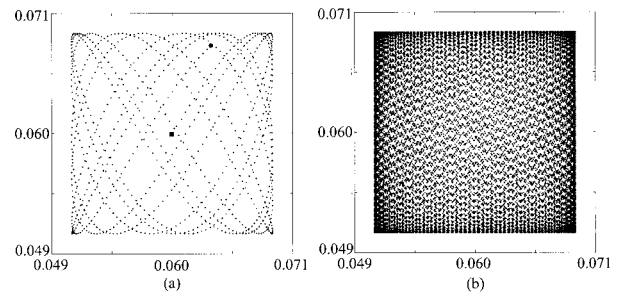

Fig. 11. Plots of assigned $\mu_a(n_1, t)$ versus $\mu_a(n_2, t)$ (cm^{-1}), where n_1 and n_2 denote two specific curved-slab FEM mesh nodes. In particular, n_1 and n_2 are those nodes for which the modulation frequencies are $2^{1/2}$ and $5^{1/2}$ Hz. (a) $\mu_a(n_1, t)$ versus $\mu_a(n_2, t)$ plot for $N_t = 1000$; enlarged round and square dots indicate first and last points in the training and calibration time series. (b) $\mu_a(n_1, t)$ versus $\mu_a(n_2, t)$ plot for $N_t = 16,384$. As N_t increases, sampled points in μ_a space constitute more complete sampling.

would seem that $N_t = N_s$ should suffice. The empirical fact that $N_t = N_s$ does not suffice is shown explicitly in Fig. 12, where the results obtained by application of deconvolution operators computed from the first 1×10^3, 6×10^3, 1.2×10^4, and 1.6×10^4 rows of $\mathbf{X}$ and $\mathbf{Y}$ to the uncorrected image of the three-inclusion hemispheric test medium [Fig. 6(a)–(c)] are presented.

These results demonstrate that the deconvolution operator is not effective unless the number of time points taken into account is more than ten times greater than the number of FEM mesh nodes. For smaller values of N_t, the corresponding points in μ_a space do not constitute a representative sample. Additional insight into the question of why it is necessary that $N_t \gg N_s$ is provided by examination of the dependence of the condition number and effective rank of $\mathbf{X}$ on N_t. Plots of the former, for both hemispheric and curved-slab media, are shown in Fig. 13(a), and the latter, for both media, are plotted in Fig. 13(b). Here, the condition number is defined as the ratio of the smallest nonzero singular value to the
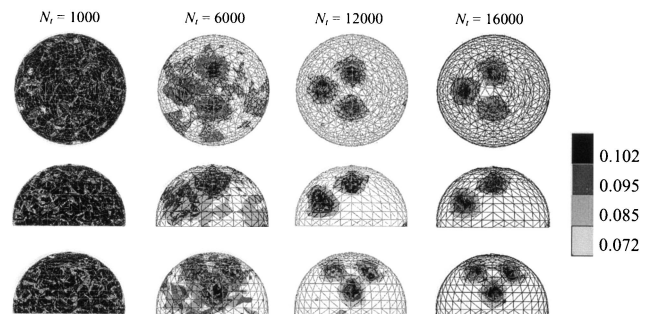

Fig. 12. Effect of the deconvolution operator applied to the reconstructed image [Figs. 6(a)–6(c)] of a three-inclusion hemispheric test medium, as a function of N_t. From left to right: results for $N_t = 10^3, 6 \times 10^3, 1.2 \times 10^4$, and 1.6×10^4. The top row shows the x–y projections; the middle row shows the x–z projections; and the bottom row shows the y–z projections of the 3D images. Numbers along the gray scale give the quantitative value of the spatially varying μ_a.
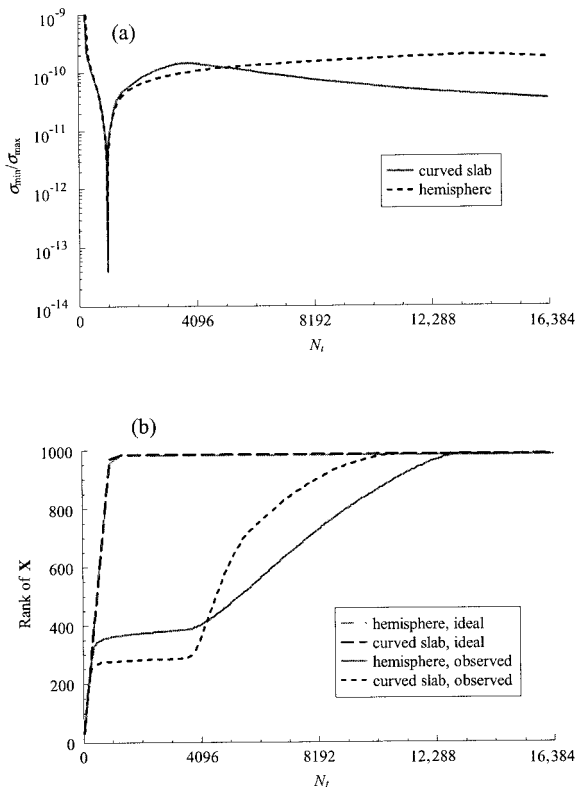
Fig. 13. Dependence of (a) condition number and (b) of the matrix **X** (defined in Subsection 2.A) on N_t. Solid curves, curved-slab target medium; dashed curves, hemispheric target medium.

largest singular value (this is the reciprocal of the usual definition, but has the advantage that the resulting quantity in constrained to lie in the interval 0.0–1.0); the closer this ratio is to zero, the more badly conditioned the matrix. Effective rank is here defined as the number of singular values larger than ε, a small positive number [in particular, ε = $10^{3/8} \times 10^{-8} \approx 2.4 \times 10^{-8}$ was used to compute the curves in Fig. 13(b)]; this is a measure of how many columns of the matrix are linearly independent. From Fig. 13(a) it is apparent that the case of $N_t = N_s$ yields the most badly conditioned **X**, from which it follows that computation of a useful **F** requires that N_t be significantly larger than N_s. At the same time it can be seen that the condition of **X** does not always improve with increasing N_t, so another factor must be involved in producing the calibration-set-length dependence that can be seen in Fig. 12. The effective rank curves in Fig. 13(b) supply the remaining piece of the puzzle. They signify that until N_t exceeds N_s by a factor of ~10, the effective rank of **X** is smaller than the number of nodes in the FEM mesh. That is, as a practical matter not all columns of **Y** can be simultaneously equated to linear combinations of the columns of **X**.

C.   Future Directions

The preceding characterizations of deconvolution operators and their mechanism of action suggest sev-

eral directions for further development and improvement of the image enhancement strategy presented in this report. For one, it appears highly probable that a simultaneously fast and accurate hybrid reconstruction algorithm can be synthesized by the application of the spatial deconvolution and a nonlinear updating scheme in an alternating fashion. The resulting procedure should converge more rapidly than, say, the LM algorithm used to generate the results shown in Fig. 10, while also permitting recovery of media in which nonlinear effects of the optical coefficient perturbations are significant. A second modification that is of equal importance, and whose implementation is more straightforward, is to tag both the absorption and the scattering coefficients of a medium simultaneously. The principal benefit of this is that the filter matrices thereby derived can be applied to the output of algorithms that provide simultaneous reconstruction of μ_a and μ_s. At the same time, it would constitute a mechanism for quantifying the extent of interparameter cross talk associated with a given reconstruction algorithm[10] and for reducing its effect where it does occur. An important conceptual point is that such cross talk can be regarded as another sort of information spread, one that occurs in optical parameter space rather than in physical space. As such, the same general strategy that is used to correct for the effects of a reconstruction algorithm's ISFs should also be able to reduce cross-talk artifacts. A third objective will be to search for nonsinusoidal forms for the tagging functions that are optimal in the sense of minimizing the N_t that is needed to achieve a representative sampling of μ_a space. In contrast to the first two tasks, this one is geared more toward reducing total computational overhead than to directly increasing the range of applicability of the method. However, it is reasonable to expect that a reduction of the overall size of the linear systems that must be solved [Eq. (3)] will assume considerable practical importance when implementation of the first and second objectives is attempted.

References

1. R. L. Barbour, H. L. Graber, C. H. Schmitz, Y. Pei, S. Zhong, S.-L. S. Barbour, S. Blattman, and T. Panetta, "Spatiotemporal imaging of vascular reactivity by optical tomography," *Proceedings of Inter-Institute Workshop on In Vivo Optical Imaging at the NIH*, A. H. Gandjbakhche, ed. (Optical Society of America, Washington, D.C., 2000), pp. 161–166.

2. C. H. Schmitz, H. L. Graber, H. Luo, I. Arif, J. Hira, Y. Pei, A. Bluestone, S. Zhong, R. Andronica, I. Soller, N. Ramirez, S.-L. S. Barbour, and R. L. Barbour, "Instrumentation and calibration protocol for imaging dynamic features in dense-scattering media by optical tomography," Appl. Opt. **39,** 6466–6486 (2000).

3. C. H. Schmitz, M. Löcker, J. M. Lasker, A. H. Hielscher, and R. L. Barbour, "Instrumentation for fast functional optical tomography," Rev. Sci. Instrum. **73,** 429–439 (2002).

4. H. L. Graber, C. H. Schmitz, Y. Pei, S. Zhong, S.-L. S. Barbour,

S. Blattman, T. Panetta, and R. L. Barbour, "Spatio-temporal imaging of vascular reactivity," in *Medical Imaging 2000: Physiology and Function from Multidimensional Images*, C.-T. Chen and A. V. Clough, eds., Proc. SPIE **3978**, 364–376 (2000).

5. R. L. Barbour, H. L. Graber, Y. Pei, S. Zhong, C. H. Schmitz, J. Hira, and I. Arif, "Optical tomographic imaging of dynamic features of dense-scattering media," J. Opt. Soc. Am. A **18**, 3018–3036 (2001).

6. G. S. Landis, T. F. Panetta, S. B. Blattman, H. L. Graber, Y. Pei, C. H. Schmitz, and R. L. Barbour, "Clinical applications of dynamic optical tomography in vascular disease," in *Optical Tomography and Spectroscopy of Tissue IV*, B. Chance, R. R. Alfano, B. J. Tromberg, M. Tamura, and E. M. Sevick-Muraca, eds., Proc. SPIE **4250**, 130–141 (2001).

7. R. L. Barbour, H. L. Graber, Y. Pei, and C. H. Schmitz, "Imaging of vascular chaos," in *Optical Tomography and Spectroscopy of Tissue IV*, B. Chance, R. R. Alfano, B. J. Tromberg, M. Tamura, and E. M. Sevick-Muraca, eds., Proc. SPIE **4250**, 577–590 (2001).

8. Y. Pei, H. L. Graber, and R. L. Barbour, "Influence of systematic errors in reference states on image quality and on stability of derived information for dc optical imaging," Appl. Opt. **40**, 5755–5769 (2001).

9. Y. Pei, H. L. Graber, and R. L. Barbour, "Normalized-constraint algorithm for minimizing inter-parameter crosstalk in DC optical tomography," Opt. Express **9**, 97–109 (2001), www.opticsexpress.org.

10. H. L. Graber, Y. Pei, and R. L. Barbour, "Imaging of spatio-temporal coincident states by DC optical tomography," IEEE Trans. Med. Imaging **21**, 852–866 (2002).

11. H. L. Graber, R. L. Barbour, and Y. Pei, "Quantification and enhancement of image reconstruction accuracy by frequency encoding of spatial information," in *Biomedical Topical Meetings, Vol. 71 of OSA Trends in Optics and Photonics Series* (Optical Society of America, Washington, D.C., 2002), pp. 635–637.

12. R. L. Barbour, H. L. Graber, Y. Xu, Y. Pei, and R. Aronson, "Strategies for imaging diffusing media," Transp. Theory Stat. Phys. **33**, 361–371 (2004).

13. R. L. Barbour, H. L. Graber, and Y. Pei, "A method for frequency encoded spatial filtering to enhance imaging quality of scattering media," U.S. provisional patent application 60/309,572 (filed 2 August 2002).

14. R. L. Barbour, H. L. Graber, Y. Pei, and Y. Xu, "Image enhancement by spatial linear deconvolution," U.S. provisional patent application 60/488,325 (filed 18 July 2003).

15. J. W. Goodman, "Imaging in the presence of randomly inhomogeneous media," in *Statistical Optics* (Wiley-Interscience, New York, 1985), Chap. 8.

16. D. Hancock, "'Prototyping' the Hubble fix," IEEE Spectrum **30**, 34–39 (1993).

17. T. J. Schulz, B. E. Stribling, and J. J. Miller, "Multiframe blind deconvolution with real data: imagery of the Hubble Space Telescope," Opt. Express **1**, 355–362 (1997), www.opticsexpress.org.

18. C. L. Matson, "Deconvolution-based spatial resolution in optical diffusion tomography," Appl. Opt. **40**, 5791–5801 (2001).

19. H. Hofer, L. Chen, Y. Yoon, B. Singer, Y. Yamauchi, and D. R. Williams, "Improvement in retinal image quality with dynamic correction of the eye's aberrations," Opt. Express **8**, 631–643 (2001), www.opticsexpress.org.

20. M. R. Ostermeyer and S. L. Jacques, "Perturbation theory for diffuse light transport in complex biological tissues," J. Opt. Soc. Am. A **14**, 255–261 (1997).

21. H. L. Graber, R. Aronson, and R. L. Barbour, "Nonlinear effects of localized absorption perturbations on the light distribution in a turbid medium," J. Opt. Soc. Am. A **15**, 838–848 (1998).

22. H. Jiang, Y. Xu, and N. Iftimia, "Experimental three-dimensional optical image reconstruction of heterogeneous turbid media," Opt. Express **7**, 204–209 (2000), www.opticsexpress.org.

23. A. Greenbaum, *Iterative Methods for Solving Linear Systems* (Society for Industrial and Applied Mathematics, Philadelphia, Pa., 1997), Section 3.5.1, pp. 13–16.

24. R. L. Barbour, S. S. Barbour, P. C. Koo, H. L. Graber, R. Aronson, and J. Chang, "MRI-guided optical tomography: prospects and computation for a new imaging method," IEEE Comput. Sci. Eng. **2**, 63–77 (1995).

25. J. P. Hipwell, G. P. Penney, R. A. McLaughlin, K. Rhode, P. Summers, T. C. Cox, J. V. Byrne, J. A. Noble, and D. J. Hawkes, "Intensity-based 2-D-3-D registration of cerebral angiograms," IEEE Trans. Med. Imaging **22**, 1417–1426 (2003).

26. S. Suzuki and S. Yamaguchi, "Comparison between an image reconstruction method of filtering backprojection and the filtered backprojection method," Appl. Opt. **27**, 2867–2870 (1988).

27. G. L. Zeng and G. T. Gullberg, "A backprojection filtering algorithm for a spatially varying focal length collimator," IEEE Trans. Med. Imaging **13**, 549–556 (1994).

28. H. L. Graber, Y. Pei, R. L. Barbour, D. K. Johnston, Y. Zheng, and J. E. Mayhew, "Signal source separation and localization in the analysis of dynamic near-infrared optical tomographic time series," in *Optical Tomography and Spectroscopy of Tissue V*, B. Chance, R. R. Alfano, B. J. Tromberg, M. Tamura, and E. M. Sevick-Muraca, eds., Proc. SPIE **4955**, 31–51 (2003).

29. B. W. Pogue, T. O. McBride, J. Prewitt, U. Österberg, and K. D. Paulsen, "Spatially variant regularization improves diffuse optical tomography," Appl. Opt. **38**, 2950–2961 (1999).

30. I. Bouchouev and V. Isakov, "Uniqueness, stability and numerical methods for the inverse problem that arises in financial markets," Inverse Probl. **15**, R95–R115 (1999).

31. T. F. Coleman, Y. Li, and A. Verma, "Reconstructing the unknown local volatility function," J. Comput. Finance **2**, 77–102 (1999).